

Frequency cycling to alleviate unknown frequency offsets for adiabatic half-passage pulses in surface nuclear magnetic resonance

Denys Grombacher¹, Raphael Dlugosch², Elliot Grunewald³, Mike Müller-Petke², and Esben Auken¹

ABSTRACT

Adiabatic half-passage (AHP) pulses show great promise for significantly enhancing the signal-to-noise ratio of the surface nuclear magnetic resonance (NMR) free-induction decay measurement. Performing an AHP requires that the frequency sweep terminates when the transmit frequency is equal to the Larmor frequency, a condition that demands accurate knowledge of the true Larmor frequency. If the frequency sweep is terminated at an incorrect frequency, i.e., with an unknown offset between the transmit and Larmor frequency at the end of the pulse, the net excitation is affected and it can differ from that predicted by modeling that assumes a 0 Hz offset at the end of the sweep. Surface NMR surveys using a traditional single-frequency pulse have previously been shown to display degraded performance in

the presence of an uncertain Larmor frequency estimate; the AHP pulse is also likely susceptible to such degraded performance. To ensure that reliable results can be produced by AHP pulses in the presence of an uncertain Larmor frequency estimate, we have developed an approach that adapts the frequency-cycling scheme for use with AHP pulses. We hypothesize that data collected using two similar AHP pulses, each with the exact same frequency sweep but where one sweeps toward the Larmor frequency from higher frequencies and the other from lower frequencies, can be stacked in such a manner that the impact of an unknown frequency offset is significantly reduced. We present synthetic and field results to demonstrate that frequency-cycling AHP pulse surface NMR data can ensure reliable performance even in the presence of an uncertain Larmor frequency estimate.

INTRODUCTION

The use of adiabatic half-passage (AHP) pulses as excitation pulses (Bendall and Pegg, 1986) in surface nuclear magnetic resonance (NMR) has been recently demonstrated to lead to dramatic increases in the signal-to-noise ratio (S/N) (Grunewald et al., 2016). Such S/N increases help to address one of the primary shortcomings of the surface NMR technique, the occurrence of low S/N signals, and show great promise to improve signal quality, decrease acquisition times, and expand the range of conditions in which surface NMR measurement is feasible. The type of adiabatic pulse previously implemented in surface NMR is an AHP (Silver et al., 1984; Garwood and Delabarre, 2001). This type of pulse involves a frequency sweep described by $\Delta\omega(t)$ that begins with the transmit

frequency (ω_t) far from the Larmor frequency (ω_0) and terminates the pulse when $\omega_t = \omega_0$; $\Delta\omega(t) = \omega_0 - \omega_t(t)$. The exact shape and duration of the frequency sweep can take many forms, but of importance is that the initial ω_t be selected far enough from ω_0 , that the sweep satisfies the adiabatic condition (Ugurbil et al., 1988) and that the sweep terminates when $\omega_t = \omega_0$. The focus of this study is on the ability to satisfy the last condition: that $\omega_t = \omega_0$ at the end of the pulse.

Ensuring that $\omega_t = \omega_0$ at the end of the pulse requires that ω_0 is estimated accurately. Several methods can be used to determine ω_0 in practice: (1) a geomagnetic map, (2) a magnetometer, or (3) an examination of the surface NMR signal's spectrum. The use of a geomagnetic map to determine the local magnitude of earth's magnetic field (\mathbf{B}_0) can provide a useful rough estimate of the expected

Manuscript received by the Editor 22 October 2017; revised manuscript received 8 March 2018; published ahead of production 06 June 2018; published online 2 August 2018.

¹Aarhus University, Hydrogeophysics Group, Department of Geoscience, Aarhus, Denmark. E-mail: denys.grombacher@geo.au.dk; esben.auken@geo.au.dk.

²Leibniz Institute for Applied Geophysics, Hannover, Germany. E-mail: raphael.dlugosch@liag-hannover.de; mike.mueller-petke@liag-hannover.de.

³Vista-Clara Inc., Mukilteo, Washington, USA. E-mail: elliot@vista-clara.com.

© 2018 Society of Exploration Geophysicists. All rights reserved.

ω_0 at a field site ($\omega_0 = \gamma|\mathbf{B}_0|$, where γ is the gyromagnetic ratio of the hydrogen nuclei). A better practice is to directly measure \mathbf{B}_0 at the site using a magnetometer. However, even direct measurements produce ω_0 estimates that can have high uncertainty. For example, ω_0 may be different at the measurement location (on the ground surface) compared with its value at the signal's spatial origin (at depth in the subsurface) or ω_0 can be temporally varying. Examination of the surface NMR signal's spectrum can also help improve the ω_0 estimate because the spectrum will exhibit a peak at the Larmor frequency, but for noisy or short-duration signals, the frequency resolution may not be sufficient to reliably determine ω_0 to the desired accuracy (Grombacher et al., 2016). This can lead to an unknown offset between the estimated Larmor frequency (denoted $\omega_{0,\text{est}}$) and the true Larmor frequency (denoted $\omega_{0,\text{true}}$); we will refer to this unknown offset as $\Delta\omega_{\text{un}}$ ($\Delta\omega_{\text{un}} = \omega_{0,\text{true}} - \omega_{0,\text{est}}$). In the following, the term offset refers to a frequency offset.

In the presence of nonzero $\Delta\omega_{\text{un}}$, the accuracy of the surface NMR forward model will be reduced (Walbrecker et al., 2011). For the standard single-frequency excitation pulses (e.g., on-resonance or off-resonance pulses), nonzero $\Delta\omega_{\text{un}}$ lead to unknown off-resonance effects that perturb the signal's amplitude, phase, and spatial origin (i.e., where in the subsurface the measured signal is located). Trushkin et al. (1993) highlight the magnitude of potential amplitude variations for the single-frequency pulse case and illustrate that the perturbations depend strongly on pulse length. Several studies have also demonstrated that neglecting these effects can lead to poor water-content profiles (Grombacher and Knight, 2015) and the appearance of phantom aquifers at depth (Legchenko, 2005). For the case of single-frequency pulses, the source of the degraded performance is that the modeling is based upon an incorrect offset (due to $\Delta\omega_{\text{un}}$). For an AHP pulse, the presence of nonzero $\Delta\omega_{\text{un}}$ would violate the condition that the pulse should terminate when $\omega_t = \omega_{0,\text{true}}$, as we accidentally terminate the pulse when $\omega_t = \omega_{0,\text{est}}$; i.e., we terminate the pulse when $\Delta\omega(t = \tau) = \Delta\omega_{\text{un}}$ instead of $\Delta\omega(t = \tau) = 0$. Therefore, nonzero $\Delta\omega_{\text{un}}$ is also likely to impact the accuracy of the water-content profiles produced by AHP pulses. The focus of this study is to characterize the impact of $\Delta\omega_{\text{un}}$ on AHP pulse-produced water-content profiles and to develop a technique to ensure that reliable AHP pulse results can be produced in the presence of nonzero $\Delta\omega_{\text{un}}$.

Several approaches to mitigate the impact of nonzero $\Delta\omega_{\text{un}}$ have been proposed, such as an updated inversion scheme in which the offset becomes an inversion parameter (Legchenko et al., 2016) and an alternate data-acquisition strategy referred to as frequency cycling (Grombacher et al., 2016). These approaches were developed in the context of single-frequency pulses, but they can likely be extended to the AHP pulse case. Our focus is to adapt the frequency-cycling scheme for implementation with AHP pulses, given that it does not require estimation of $\Delta\omega_{\text{un}}$, but rather collects data in such a manner as to directly mitigate its influence. The frequency-cycling approach for the single-frequency pulse case requires combining two off-resonance data sets, in which ω_t in each data set was set to equal-magnitude positive and negative offsets about $\omega_{0,\text{est}}$. For frequency cycling with AHP pulses, we propose to combine two data sets produced using an AHP pulse that sweeps toward $\omega_{0,\text{est}}$ from lower frequencies (referred to as sweeping from below) and a second data set produced using an AHP pulse that sweeps toward $\omega_{0,\text{est}}$ from higher frequencies (referred to as sweeping from above). This approach is similar to that discussed by Grunewald et al.

(2016), where it was proposed to eliminate the oscillatory in-phase component of the AHP pulse signal. Our aim is to preserve the in-phase (real) and out-of-phase (imaginary) components of the AHP signal while simultaneously mitigating the influence of a nonzero $\Delta\omega_{\text{un}}$, with the ultimate goal of ensuring a reliable forward model. Synthetic and field studies of frequency cycling for AHP pulses are presented to demonstrate the feasibility of the approach and identify limits for which nonzero $\Delta\omega_{\text{un}}$ can be mitigated.

BACKGROUND

To generate a measurable NMR signal, an excitation pulse is used to perturb the subsurface magnetization out of its equilibrium orientation. Following the perturbation, the component of the magnetization transverse to the direction of \mathbf{B}_0 , called the transverse magnetization m_{\perp} , can be inductively measured by a coil at the surface (Semenov et al., 1989). Reliable forward modeling of the surface NMR signal requires that the potential transverse magnetization at each location in the subsurface be modeled accurately. This involves solving the Bloch equation at each location in the subsurface, given the local amplitude of the applied magnetic field ($B_1(t)$) and the current waveform $I(t)$ describing the excitation pulse. Note that the use of B_1 here refers to the corotating component of the applied magnetic field perpendicular to earth's field (Weichmann et al., 2000). The Bloch equation is

$$\frac{d\mathbf{M}}{dt} = \gamma\mathbf{M} \times \mathbf{B}_{\text{eff}} - \frac{M_x}{T_2}\mathbf{x} - \frac{M_y}{T_2}\mathbf{y} - \frac{M_z - M_0}{T_1}\mathbf{z}, \quad (1)$$

and it describes the perturbation of the magnetization \mathbf{M} due to a magnetic field \mathbf{B}_{eff} and relaxation described by the relaxation times T_2 and T_1 . The \mathbf{B}_{eff} field is given by

$$\mathbf{B}_{\text{eff}}(t) = \begin{bmatrix} B_1(t) \\ 0 \\ \Delta\omega(t)/\gamma \end{bmatrix}. \quad (2)$$

Equation 2 describes the \mathbf{B}_{eff} field in a reference frame that rotates at the instantaneous transmit frequency and whose x - and z -axes are oriented in the direction of the component of \mathbf{B}_1 perpendicular to \mathbf{B}_0 , and the \mathbf{B}_0 direction, respectively. We must solve equation 1 from $t = 0$ until $t = \tau$ (τ is the pulse duration), given the initial condition of a unit magnetization at equilibrium. The transverse component of \mathbf{M} (i.e., M_x and M_y) enters the surface NMR forward model through the term $m_{\perp} = M_y + iM_x$. This complex-valued representation, where M_y is treated as the real component and M_x as the imaginary component, is the convention in surface NMR.

For a single-frequency pulse, where ω_t is a constant, \mathbf{B}_{eff} is static as its x - and z -components do not vary during the pulse. In contrast, for an adiabatic pulse, the magnitude and orientation of \mathbf{B}_{eff} vary during the pulse because of the varying transmit frequency and B_1 strength (i.e., varying z - and x -components in equation 2, respectively). Previous implementations of AHP pulses in surface NMR have used tuned transmit coils that result in passive modulation of the B_1 amplitude. In this case, the current amplitude $I(t)$ (and therefore $B_1(t)$) is linked to $\Delta\omega(t)$ via the frequency response of the tuned transmit coil. For an excitation pulse to be a strict AHP, the adiabatic pulse type most effective at producing a large transverse magnetization, the pulse must satisfy three conditions (Tannus and Garwood, 1997):

- 1) The initial ω_i must be selected such that \mathbf{B}_{eff} is oriented nearly parallel to \mathbf{B}_0 .
- 2) The frequency sweep must satisfy the adiabatic condition at all times.
- 3) The pulse must terminate when \mathbf{B}_{eff} is oriented in the transverse plane.

Condition 1 ensures that the magnetization vector and the \mathbf{B}_{eff} vector are nearly colinear at the onset of the pulse; the magnetization will therefore precess about a small cone centered on the \mathbf{B}_{eff} vector. Condition 2 states that the rate of change of the \mathbf{B}_{eff} vector's orientation is much smaller than the rate that the magnetization precesses about \mathbf{B}_{eff} ; this ensures that the magnetization remains locked to the \mathbf{B}_{eff} vector. The final condition ensures that if the magnetization vector's orientation remains locked to the \mathbf{B}_{eff} direction, the magnetization will end the pulse in the transverse plane, thus maximizing its contribution to the NMR signal. If conditions 1 and 2 are satisfied but condition 3 is not, the magnetization will not be fully oriented in the transverse plane at the end of the pulse. This has the potential to impact the amplitude and phase of the measured signal.

In the following synthetic cases, we neglect the relaxation terms in equation 1, which is equivalent to solving the Bloch equation in the no relaxation during pulse limit. This represents the standard modeling approach currently used in surface NMR (Weichman et al., 2000) and will facilitate a more straightforward examination of the impact of $\Delta\omega_{\text{un}}$.

RESULTS

Impact of an unknown offset on a surface NMR survey using an AHP pulse

The top cluster of Figure 1 illustrates the transverse magnetization components produced by hyperbolic tangent AHP described by $\Delta\omega(t) = A(1 - (\tan h(\eta t/\tau) / \tan h(\eta)))$, where $A/2\pi = 100$ Hz, $\eta = 3$, and $\tau = 60$ ms. This particular pulse is chosen because it has a simple analytic description of the frequency sweep. It serves to demonstrate the typical behavior of an AHP pulse in surface NMR. Figure 1a and 1c illustrates the M_x and M_y components produced at the end of this example pulse over a range of B_1 typical of that present in surface NMR. To form each point in the curves, equation 1 is solved using a fourth-order Runge-Kutta solver to determine the M_x and M_y components given an initial condition of a unit magnetization at equilibrium, the relevant B_1 amplitude, and a $\mathbf{B}_{\text{eff}}(t)$ vector corresponding to the hyperbolic tangent pulse. The solver allows the magnetization at time t_{i+1} to be estimated based on the magnetization at time t_i and the update described by equation 1. To approximate $\mathbf{B}_{\text{eff}}(t)$ during the frequency sweep, $\mathbf{B}_{\text{eff}}(t)$ is treated as a series of discrete values that are updated at each time step. The colors in each subplot correspond to a particular $\Delta\omega_{\text{un}}$. The M_x profiles (Figure 1a) are described by a large positive bump, which corre-

sponds to the range of B_1 , where \mathbf{M} remained mostly locked to the \mathbf{B}_{eff} vector during the pulse. If the pulse perfectly satisfies all of the above three conditions, an M_x component of one is produced. The M_y component is described by a large bump at lower B_1 , followed by strongly oscillatory behavior at large B_1 . This oscillatory behavior is mainly a consequence of not satisfying condition 1 well, leading to the precession about a large cone, which results in a large M_y component. Figure 1b and 1d illustrates the difference between each M_x and M_y profile and the $\Delta\omega_{\text{un}} = 0$ (black) profile. Given that $\Delta\omega_{\text{un}}$ by definition is unknown, modeling would likely be performed assuming that $\Delta\omega_{\text{un}} = 0$. Therefore, Figure 1b and 1d illustrates the potential magnitude of excitation modeling errors introduced by $\Delta\omega_{\text{un}}$. The main effect of nonzero $\Delta\omega_{\text{un}}$ appears to be focused around B_1 values, where the initial rise of the M_x and M_y profiles occurs. The difference grows with increasing $\Delta\omega_{\text{un}}$, where the residual can be positive or negative depending on the sign of $\Delta\omega_{\text{un}}$. At larger B_1 , the differences are reduced.

Although Figure 1a–1d provides insight into the impact of $\Delta\omega_{\text{un}}$ on the net excitation, the m_{\perp} profiles alone are insufficient to determine the expected impact on the surface NMR signal. This requires solution of the full surface NMR forward problem, in which the $m_{\perp}(B_1)$ profiles are mapped into the subsurface to model the expected signal amplitudes. The bottom cluster of Figure 1e–1h illustrates the sounding curves (initial signal amplitudes as a function of the pulse current amplitude) produced by the same hyperbolic tangent pulse for the same range of $\Delta\omega_{\text{un}}$. The sounding

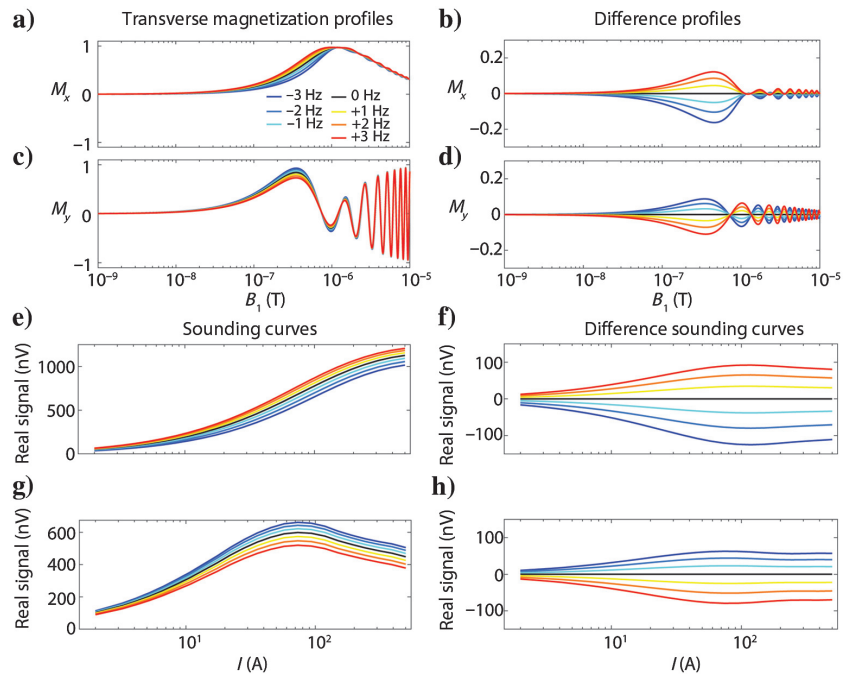


Figure 1. (a and c) Illustrate the M_x and M_y components produced by a hyperbolic tangent pulse of 60 ms duration, $A/2\pi = 100$ Hz, and $\eta = 3$ for a range of different unknown offsets (colors). The relevant unknown offset for each color is shown in the legend. (b and d) Illustrate the difference between the M_x and M_y profiles for each unknown offset compared with the 0 Hz unknown offset case. (e and g) Illustrate the imaginary and real sounding curves for a synthetic survey using the same pulse as in (a-d), a 60 m circular coincident loop, and a resistive 30% water-content half-space for the same range of unknown offsets investigated in (a-d). (f and h) Illustrate the difference between the imaginary and real sounding curves for each unknown offset compared with the 0 Hz unknown offset case.

curves correspond to synthetic surveys using a 60 m circular coincident loop, with a resistive 30% water-content half-space. Forward modeling was performed using MRSmatlab (Müller-Petke et al., 2016). The conductivity term in the forward model used in this work is based on a single frequency (the frequency at the end of the pulse). Although the dependence of the sounding curves on the offset will in practice depend on the specific subsurface water-content profile, this simple 30% water-content half-space example provides useful insight into the potential magnitude of the sensitivity to the unknown offset. Figure 1e and 1g illustrates the imaginary and real sounding curves, respectively. To emphasize the impact of $\Delta\omega_{\text{un}}$ on the sounding curves, Figure 1f and 1h illustrates the difference between the sounding curves produced by each $\Delta\omega_{\text{un}}$ and that produced when $\Delta\omega_{\text{un}} = 0$ (black). The difference sounding curves show significant amplitude variations (up to ± 100 nV), producing larger and smaller amplitudes (compared with $\Delta\omega_{\text{un}} = 0$) depending on the sign of $\Delta\omega_{\text{un}}$. Notice also that the signs of the difference signals are different for the imaginary and real components (e.g., the red difference profile is positive and negative for the imaginary and real cases, respectively). In summary, the presence of nonzero $\Delta\omega_{\text{un}}$ can lead to significant real/imaginary signal-amplitude variations when using an AHP pulse, just as in the single-frequency pulse case (Grombacher and Knight, 2015). Similar behavior was also observed for alternative AHP pulses described by linear frequency sweeps or frequency sweeps determined by the numerically optimized modulation approach (Grombacher, 2018) (not shown). In a later section, we investigate if and how these signal variations affect the accuracy of the estimated water-content profiles.

Impact of an unknown offset on a survey using an AHP pulse and frequency cycling

Given that nonzero $\Delta\omega_{\text{un}}$ are by definition difficult to detect and are capable of significant signal amplitude/phase perturbation, an

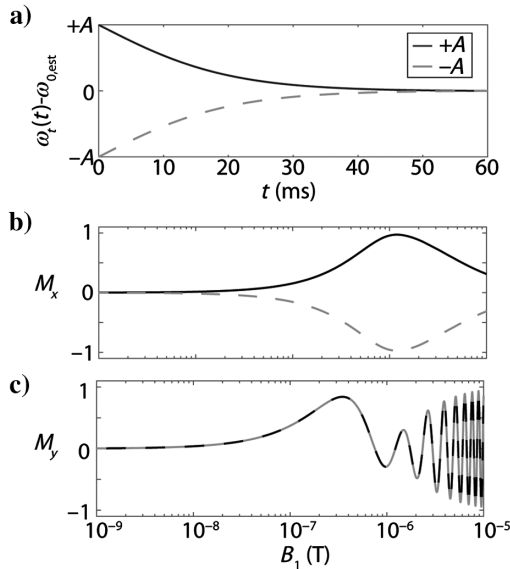


Figure 2. (a) The frequency sweeps for the +A (black) and -A (dashed gray) cases. (b and c) Illustrate the M_x and M_y components produced by the same hyperbolic tangent pulse investigated in Figure 1, but where the black line corresponds to +A and the dashed gray line corresponds to -A. Note that alternating the sign of A alters the sign of the M_x component, while leaving the M_y component unaffected.

approach capable of directly mitigating their influence is highly desirable. We propose to adapt the frequency-cycling approach for use with AHP pulses. We propose a data-acquisition scheme in which data are collected using two similar AHP pulses, where the first corresponds to a positive initial offset (i.e., +A sweeps from above $\omega_{0,\text{est}}$) and a second corresponds to a negative initial offset (i.e., -A sweeps from below $\omega_{0,\text{est}}$). The +A and -A data sets will be referred to as d_{+A} and d_{-A} , respectively. Figure 2a illustrates the differences between the frequency sweeps for the d_{+A} (black line) and d_{-A} (dashed gray line) cases. In each case, the shape of the frequency sweep is identical, but the sweep direction is reversed with both cases converging toward $\omega_{0,\text{est}}$ at the end of the sweep. If an unknown offset is present, both sweeps will terminate with $\Delta\omega(t = \tau) = \Delta\omega_{\text{un}}$ instead of the desired condition $\Delta\omega(t = \tau) = 0$. Note that for the frequency-cycling approach $\omega_{0,\text{true}}$ does not directly enter the modeling or pulse design, instead $\omega_{0,\text{est}}$ is sufficient. The purpose of this approach is to alter the sign of one of the real or imaginary components of the signal (in this case, the imaginary component), allowing them to be stacked in a manner that constructively stacks the signal well-described by modeling that assumes $\Delta\omega_{\text{un}} = 0$, while simultaneously destructively stacking the portion of the signal that arises from the nonzero $\Delta\omega_{\text{un}}$. The +A hyperbolic tangent pulse will produce the M_x and M_y profiles shown by the solid black lines in Figure 2b and 2c, whereas the -A hyperbolic tangent pulse will produce the M_x and M_y profiles shown by the dashed gray lines in Figure 2b and 2c. Note that changing the sign of A changes the sign of the M_x component (which corresponds to the imaginary component of the data), whereas the sign of the M_y component is unchanged (which corresponds to the real component of the data). To form the frequency-cycled data (d_{FC}), the two individual data sets are combined using equation 3:

$$d_{\text{FC}} = (\text{real}(d_{+A} + d_{-A}) + i * \text{imag}(d_{+A} - d_{-A}))/2. \quad (3)$$

For each $\Delta\omega_{\text{un}}$, the +A and -A scenarios always terminate at the same frequency— $\omega_{0,\text{est}}$. Of importance is that one of the scenarios involves sweeping past $\omega_{0,\text{true}}$, whereas the other scenario terminates the sweep before reaching $\omega_{0,\text{true}}$.

To demonstrate that data stacked using equation 3 can help to improve the accuracy of the forward model that assumes $\Delta\omega_{\text{un}} = 0$, the top cluster of Figure 3 illustrates the M_x and M_y profiles produced by the frequency-cycling approach for the same AHP pulse and suite of $\Delta\omega_{\text{un}}$ investigated in Figure 1. The M_x and M_y profiles for the nonzero $\Delta\omega_{\text{un}}$ cases are formed using equation 3 (where real corresponds to the M_y component and imaginary to the M_x component). In this case, the M_x and M_y profiles (Figure 3a and 3c) track one another closely. The difference profiles (i.e., the difference between the M_x and M_y profiles for each $\Delta\omega_{\text{un}}$ and the profiles for $\Delta\omega_{\text{un}} = 0$) are very close to zero over the full range of investigated B_1 . Note that the negative-offset profiles (dark to light blue) are overlain by the positive-offset profiles (yellow to red) of the same magnitude offset. This indicates that the frequency-cycling approach is likely to produce accurate excitation modeling even in the presence of a nonzero $\Delta\omega_{\text{un}}$; this suggests that knowledge of only $\omega_{0,\text{est}}$ is sufficient for accurate modeling. To investigate the impact of nonzero $\Delta\omega_{\text{un}}$ on the expected surface NMR signal, the bottom cluster of Figure 3e–3h illustrates the sounding curves for the same AHP pulse, survey/subsurface conditions, and range of $\Delta\omega_{\text{un}}$ investigated in Figure 1. In this case, the imaginary and real sounding curves track one another closely (Figure 3e and 3g). The difference

between the sounding curves produced in the presence of nonzero $\Delta\omega_{\text{un}}$ compared with the $\Delta\omega_{\text{un}} = 0$ case is also significantly reduced (Figure 3f and 3h). The negative-offset sounding curves (dark to light blue) are again overlain by the positive-offset sounding curves (yellow to red) of the same magnitude offset. Comparing Figure 3 with Figure 1 highlights that the frequency-cycling approach is likely to produce much more robust modeling in the presence nonzero $\Delta\omega_{\text{un}}$ compared with the alternative strategy of neglecting its presence (the current standard). Note that the scales in Figure 3f and 3h are much smaller (spanning 30 nV total) than in Figure 1f and 1h (which spans 300 nV total). Although Figure 3 suggests that using the frequency-cycling approach can improve the performance, the ultimate test is whether frequency cycling can ensure that more reliable water-content profiles are produced.

To investigate the potential impact of an unknown offset on the estimated water-content profiles for surveys using an AHP pulse, the results for a suite of synthetic surveys are presented. Each survey uses the same survey geometry/parameters as that used to produce the sounding curves in Figures 1 and 3, in which the difference now is that different subsurface water-content profiles are used. The same range of unknown offsets is also investigated. In each case, data are forward modeled for the relevant $\Delta\omega_{\text{un}}$, and then subsequently inverted using a kernel that assumes $\Delta\omega_{\text{un}} = 0$. This represents the scenario in which data were unknowingly collected in the presence of nonzero $\Delta\omega_{\text{un}}$, but the inversion is performed under the assumption that $\Delta\omega_{\text{un}} = 0$. We will refer to this scenario as the “standard approach,” which reflects how data with an unknown offset present would be typically handled. All inversions in this study use the QT-inversion scheme (Mueller-Petke and Yaramanci, 2010). To form frequency-cycled data, two synthetic data sets (one for $+A$, one for $-A$) are combined using equation 3. Gaussian white noise with a standard deviation of 50 nV is added to all synthetic data. Figures 4 and 5 present the estimated water-content profiles (for each $\Delta\omega_{\text{un}}$) for three different subsurface models (each column represents a particular subsurface model). The first model (left column) is a 30% water-content half-space representative of a thick unconfined aquifer. The second model (middle column) is a two-layer system that represents a 15 m thick unconfined aquifer underlain by a low-water-content layer. The third model represents a three-layer system consisting of a 10 m thick water-bearing layer present in a low-water-content half-space. In each of the three synthetic cases, layers with 30% water content have $T_2^* = 200$ ms whereas the lower water-content layers have $T_2^* = 50$ ms. The dashed black lines in each case represent the true water-content profile. The top and middle rows illustrate the estimated water-content profiles produced using the standard approach (i.e., neglecting $\Delta\omega_{\text{un}}$) and the frequency-cycling approach, respectively. The bottom row illustrates the data fit (error weighted χ^2) in each case. Figures 4 and 5 illustrate the results produced by an ampli-

tude-only inversion and a complex inversion, respectively. For the complex inversion, the real and imaginary components are inverted simultaneously but are treated separately. That is, the data vector for the complex case is defined as $\mathbf{d} = [\text{real}(\mathbf{d}); \text{imag}(\mathbf{d})]$, and the kernel matrix $\mathbf{K} = [\text{real}(\mathbf{K}); \text{imag}(\mathbf{K})]$ (Irons and Li, 2014; Müller-Petke et al., 2016), where the resulting \mathbf{d} and \mathbf{K} are real valued. This separation is a convenient approach to constrain the estimated water contents to be real valued (instead of having complex-valued water contents that are unphysical).

Consider first the amplitude-only inversion results that use the standard approach, in which an unknown offset is present (the top row of Figure 4). Note that the term amplitude-only inversion in this manuscript refers to an inversion framework, in which a phase correction is applied to the data such that the imaginary component contains only noise. The inversion is then performed on the remaining real component of the full QT data cube. For the half-space example (left column), $\Delta\omega_{\text{un}}$ primarily affects the water content at depth leading to either increased or decreased water contents depending on the sign of $\Delta\omega_{\text{un}}$. Note that the data are fit well in all cases (Figure 4g), leaving little reason to suspect the presence of nonzero $\Delta\omega_{\text{un}}$. In the middle column, $\Delta\omega_{\text{un}}$ primarily affects the ability to accurately resolve the bottom of the upper high-water-content layer. However, the presence of nonzero $\Delta\omega_{\text{un}}$ is again

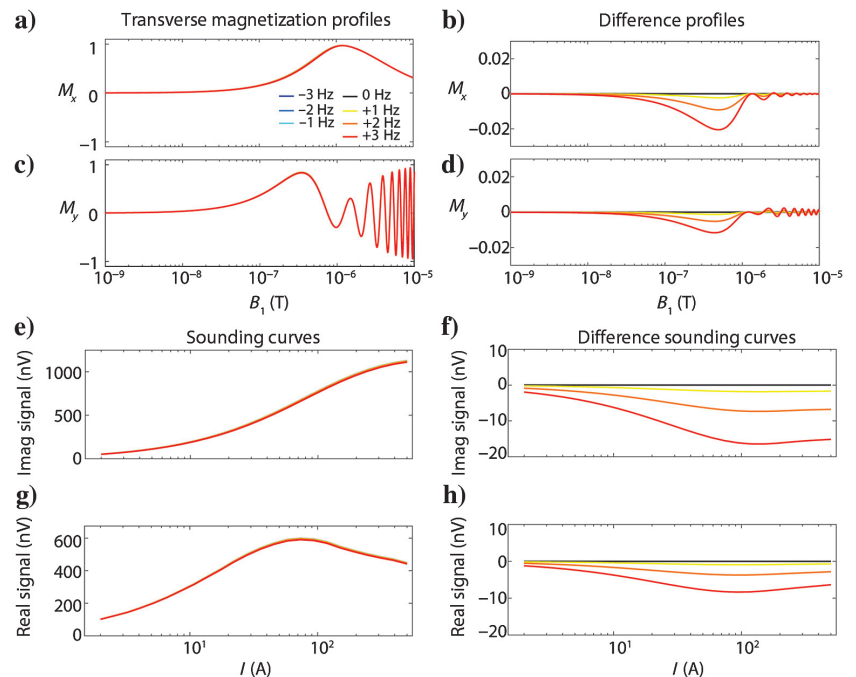


Figure 3. (a and c) Illustrate the M_x and M_y components produced using a frequency-cycling approach for a range of different unknown offsets (colors), where two hyperbolic tangent pulses of 60 ms duration and $\eta = 3$, but with alternating signs of A ($A/2\pi = \pm 100$ Hz) are combined using equation 3 (M_x and M_y are treated as the imaginary and real components, respectively). (b and d) Illustrate the difference between the frequency-cycled M_x and M_y profiles for each unknown offset compared with the 0 Hz unknown offset case. (e and g) Illustrate the imaginary and real frequency-cycled sounding curves for a synthetic survey using the same pulse as in (a-d), a 60 m circular coincident loop, and a resistive 30% water-content half-space for the same range of unknown offsets investigated in (a-d). (f and h) Illustrate the difference between the imaginary and real frequency-cycled sounding curves for each unknown offset compared with the 0 Hz unknown offset case. Note that the blue lines are mostly overlain by the yellow/red lines of equal magnitude offset.

not indicated by the data fit given that the data fit is good for all cases (Figure 4h). For the three-layer case (right column), $\Delta\omega_{\text{un}}$ also leads to challenges identifying the layer boundaries correctly, where elevated water-contents at depth are estimated in some cases (e.g., red profile). In this case, good data fits are still produced for all investigated $\Delta\omega_{\text{un}}$. The frequency-cycling profiles (middle row) in each column track one another much more closely, producing reliable water-content profiles and good data fits for all investigated scenarios.

Consider next the complex-inversion results that use the standard approach (top row of Figure 5). For the half-space example (left column), the standard results do a better job (compared with the amplitude-only inversion) of consistently reproducing the true models, in which some increased water contents are observed at depth for larger $\Delta\omega_{\text{un}}$. In the two-layer case, for negative offsets (blue), the standard inversion produces an elevated water content above the lower boundary of the upper layer, whereas the positive offsets result in elevated water contents at depth. However, in this case, the data fit is reduced for the largest investigated $\Delta\omega_{\text{un}}$ (observed by noting the increased χ^2 values in Figure 5h). Note that the water-content profiles that correspond to reduced data fits would likely be treated with greater uncertainty in practice. In these cases, a practitioner may even be prevented from using the complex inversion forcing them to use an amplitude-only inversion (because the data fits are more robust for the amplitude inversion compared with the complex inversion; e.g., compare Figures 4h and 5h). For the three-layer model, nonzero $\Delta\omega_{\text{un}}$ primarily affects the water-content

estimates in the bottom two layers for the standard case. Negative offsets (blue) overestimate the water content in layer two, whereas positive offsets underestimate the water content in layer two and overestimate the water content in layer three. Consider next the complex-inversion results for the frequency-cycling cases (middle row). The frequency-cycling results again accurately reproduce the true water-content profiles and provide robust data fits for all investigated $\Delta\omega_{\text{un}}$. Comparing the frequency-cycling results in Figures 4 and 5 also indicates that the true models are more sharply reproduced by the complex-inversion, which is consistent with [Braun and Yaramanci \(2005\)](#); e.g., the two- and three-layer models are more accurately resolved using the complex inversion compared with the amplitude-only inversion.

In summary, the proposed frequency-cycling approach for AHP pulses is expected to significantly mitigate sensitivity to nonzero $\Delta\omega_{\text{un}}$, thus providing more reliable estimates of the water-content profiles and a better ability to fit complex data. Reliable complex-data fits may also help facilitate broader exploitation of the complex-inversion, which itself brings resolution advantages ([Braun and Yaramanci, 2005](#)).

Field verification of frequency-cycling for AHP pulses

To demonstrate the feasibility of the frequency-cycling approach for AHP pulses under field conditions, several data sets were collected at the hydrogeologic test site Schillerslage near Hanover, Germany. The site has been extensively characterized previously ([Mueller-Petke and Yaramanci, 2010](#); [Dlugosch, 2014](#)), and it is known to be described by a two-aquifer system underlain by a marl bedrock at approximately 20 m depth. Figure 6a illustrates a lithology log of the site. The upper unconfined sandy aquifer begins at approximately 2 m depth and extends to approximately 11 m depth and contains a thin peat/silt layer at approximately 6 m depth. An aquiclude of tills interbedded with thin sand layers begins at approximately 11 m extending to approximately 17 m depth. The second aquifer consists of medium sands extending from 17 down to 20 m depth. The survey geometry consisted of a 60 m circular coincident transmit/receive loop. The Larmor frequency was observed to be 2104 Hz and remained within ± 0.4 Hz of this value throughout the survey. Eleven separate surface NMR data sets were recorded using the GMR instrument from Vista Clara Inc. Ten surveys used a 60 ms hyperbolic tangent AHP pulse with a 100 Hz initial offset and $\eta = 3$ (same pulse as in the previous figures) and passive current modulation. Current modulation is included in the pulse modeling by adjusting the x -component of $\mathbf{B}_{\text{eff}}(t)$ to vary with the amplitude of the pulse envelope. Five pulses swept from below resonance ($-A$), whereas another five swept from above resonance ($+A$) allowing five frequency-cycled data sets to be formed. For each sweep direction, data were collected for AHP pulses that terminated their sweeps at 2101, 2103, 2104, 2106, and 2108 Hz, which correspond to final offsets of +3, +1, 0, -2, and

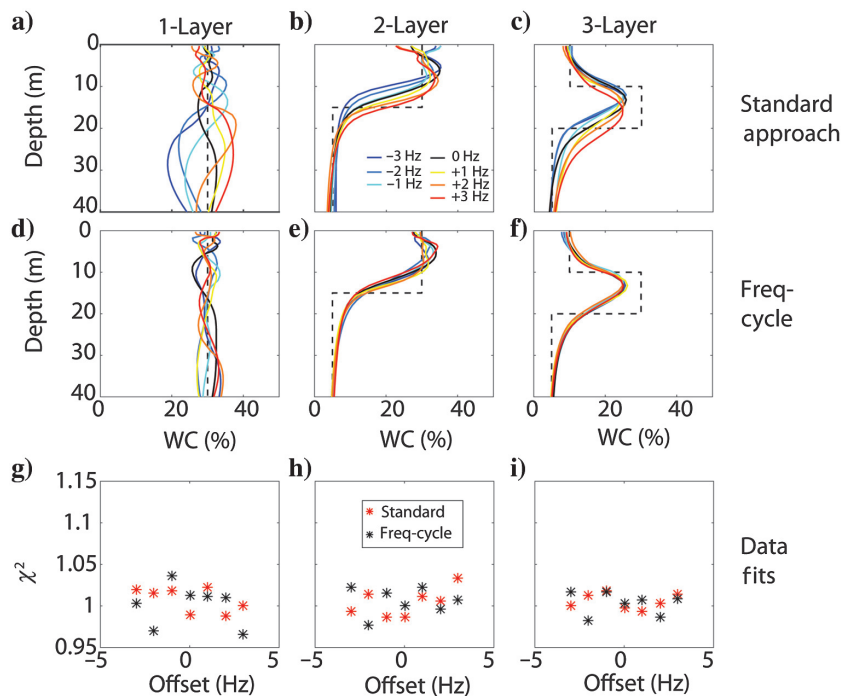


Figure 4. Water-content profiles (top two rows) and the corresponding data fits (bottom row) for amplitude-only inversions conducted in the presence of a range of unknown offsets (same offsets and colors as in Figures 1 and 3). The top row illustrates the water-content profiles produced by the standard approach that assumes no unknown offset is present, whereas the middle row shows the results for inversions that use frequency-cycling. The corresponding T_2^* profiles are not shown. Each column corresponds to a different subsurface water-content structure, in which the dashed black line shows the true water-content profile in each case.

−4 Hz, respectively. Although these final offsets are known precisely, inverting each of these data sets using a forward model that assumes the frequency sweep ended on resonance allows us to simulate the presence of unknown offsets equal to +3, +1, 0, −2, and −4 Hz. The final data set used a single frequency 40 ms on-resonance excitation pulse and the corresponding inversion result is treated as a reference. In all cases, the inverted data contain approximately 30 stacks (± 2 stacks depending on the data set). The AHP data sets used either 28 or 32 pulses with maximum current amplitudes that ranged approximately from 5 to 450 A in logarithmic steps. The on-resonance data set used 22 pulse current amplitudes, more commonly referred to as pulse moments. Table 1 outlines the details of all 11 data sets and how they were combined to form the five frequency-cycled data sets.

Prior to frequency-cycling each stacked data set (i.e., combining d_{+A} and d_{-A} data sets using equation 3 to form a single frequency-cycled pair), a phase correction ϕ_{cor} is applied to each data set used to form the frequency-cycled pair. The same phase correction is applied to d_{+A} and d_{-A} . This phase correction is necessary to account for any signal phase originating from the instrument or data processing (e.g., phases imparted by filters, phases that arise due to the particular pulse waveform, or phases that accumulate over the dead time). The phase correction is estimated by performing preliminary complex inversions on all 11 data sets individually to estimate the processing phase (ϕ_{proc} in Table 1) in each case. The two processing phase estimates (for d_{+A} and d_{-A}) are averaged to determine the phase correction ϕ_{cor} that is subsequently applied to d_{+A} and d_{-A} prior to frequency cycling. This approach was observed to work well for data collected using the GMR data-acquisition software, which has a stable instrument phase and is capable of interleaving multiple pulse types (e.g., −A and +A AHP pulses). The processing phase was observed to be relatively constant during this style of acquisition. If the processing phase cannot be kept constant for the data sets that will be frequency cycled, the phase correction can be estimated individually using the approach discussed by Grombacher et al. (2016). Alternatively, if a more explicit handling of the processing phase is performed, where each contribution to the processing phase is calibrated or determined a priori, this phase correction is unnecessary. Inversions for the field data were performed using a complex inversion with a QT-inversion scheme and a forward model that solves the full-Bloch equation until the end of the dead time (11 ms in this case) (Grombacher et al., 2017). This dead time is due to a combination of the 5 ms instrument dead time and the filter bandwidths. The alternative forward model is used because a forward model that solves the Bloch equation without relaxation terms present and uses an extrapolation to mid-pulse or extrapolation to end-pulse approach is expected to not perform as well for the hyperbolic tangent pulse (Grombacher et al., 2017). To solve the full Bloch equation, the relaxation terms are weighted using a

representative T_2^* observed at the site ($T_2^* = 300$ ms) and an estimate of $T_2 = T_1 = 500$ ms obtained from laboratory NMR measurements on samples collected at the site (Dlugosch, 2014). Although these values are estimates of representative values for the site, inversions performed for alternative T_2 estimates ranging from 350 to 900 ms were not observed to have a significant impact on the overall data fit or the estimated water-content profiles (likely because T_2^* and T_2 at the site are much longer than the pulse duration). The measured current waveform of the excitation pulse was also used in the forward modeling (Dlugosch and Müller-Petke, 2017).

Figure 6b and 6c illustrates the water-content and T_2^* profiles estimated at the site for the six data sets described in Table 1. The black lines correspond to the five frequency-cycled data sets, whereas the gray line corresponds to the 40 ms on-resonance case. The dashed black line corresponds to the frequency-cycled case with an offset of −4 Hz; the data fit in this case is reduced, and the water-content profile should be treated with greater uncertainty. Overall, all profiles accurately predict the depth to the top of the upper aquifer (approximately 2–3 m) and contain a thick high-water-content layer with long T_2^* extending to approximately 10 m depth. At less than approximately 10 m, the water content begins to drop at depths where tills interbedded with medium sands are expected. At less than approximately 20 m, the water content is reduced (approximately <5%), which is consistent with expectations that the bedrock begins at this depth. All profiles cannot clearly

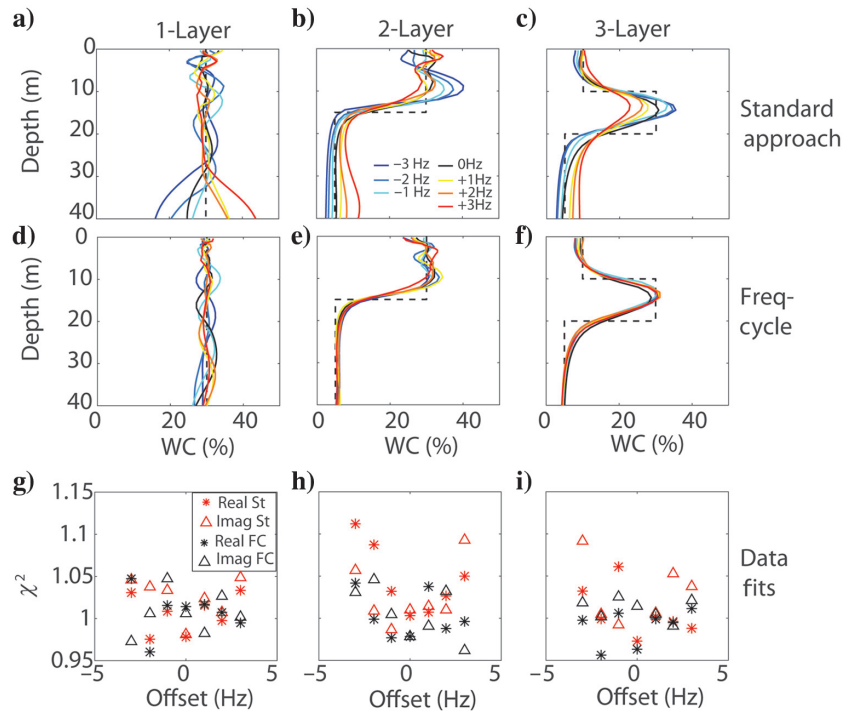


Figure 5. Water-content profiles (top two rows) and the corresponding data fits (bottom row) for complex inversions conducted in the presence of a range of unknown offsets (same offsets and colors as in Figures 1, 3, and 4). The top row illustrates the water-content profiles produced by the standard approach that assumes no unknown offset is present, whereas the middle row shows the results for inversions that use frequency-cycling. The corresponding T_2^* profiles are not shown. Each column corresponds to a different subsurface water-content structure, in which the dashed black line shows the true water-content profile in each case. The stars and triangles in the bottom row correspond to the real and imaginary data fits in each case.

differentiate between the till interbedded with medium sands layer (approximately 11–17 m) and the second aquifer (approximately 17–20 m). Note the consistency between the four solid black lines, which demonstrates the four frequency-cycling cases in which the data are fit well and produce very similar results despite the presence of unknown offsets in three of the cases. The four curves all track one another closely over the full depth range showing only minor differences; in particular, there is a small discrepancy about the estimated depth of the upper aquifer (e.g., 2 or 3 m depth) and an approximate 50 ms difference in the estimated T_2^* at an approximate 8 m depth. To illustrate the data quality and data fit, Figure 6d and 6f displays the imaginary and real frequency-cycled data set for the +3 Hz unknown offset case (i.e., $d_{FC,1}$ in Table 1). Figure 6e and 6g illustrates the forward modeled data corresponding to the relevant water-content/ T_2^* profiles in Figure 6b and 6c, respectively. The smallest and largest current indices correspond to the smallest and largest investigated currents (logarithmically spaced approximately from 5 to 450 A). The time gates are logarithmically increasing; the first and last time gates are centered at $t = 0$ and 0.86 s (after the end of the 11 ms dead time). The forward-modeled data accurately reproduce the measured data despite the fact that the $d_{FC,1}$ is collected in the presence of a +3 Hz offset and that $d_{modeled}$ assumes a 0 Hz offset. To better illustrate the quality of the data fit for all scenarios in Figure 6b and 6c, Figure 7 illustrates the real and

imaginary data misfits ($d_{measured} - d_{modeled}$) for all six data sets described in Table 1. The left and right columns correspond to the real and imaginary data misfits, respectively. Overall, the frequency-cycling inversions produce robust data fits in the upper four cases, in which the misfits are well-described by random red/blue patches. Some structure is observed in the +3 Hz case, in which the early times in the real component show a slight blue bias. The -4 Hz offset case shows the most significant structure, in which its imaginary misfit contains a positive lobe and a negative lobe. These lobes are the reason that its profile in Figure 6 should be treated with greater uncertainty. Overall, the consistency in the water-content and T_2^* profiles in Figure 6 and the data fits in Figure 7 demonstrate the feasibility of the frequency-cycling approach for AHP pulses in surface NMR.

DISCUSSION

Whether uncertainty in the estimated Larmor frequency stems from temporal \mathbf{B}_0 variations, spatial \mathbf{B}_0 variations, limited

Table 1. Description of the AHP data sets (d_{+A} and d_{-A}) used to form each frequency-cycled data set and the on-resonance data set inverted to form the profiles shown in Figure 6 and misfits illustrated in Figure 7.

	$\Delta\omega_{un}/2\pi$	d_{+A}	d_{-A}
$d_{FC,1}$	+3 Hz	Tanh	Tanh
		$A/2\pi = +100$ Hz	$A/2\pi = -100$ Hz
		$\phi_{proc} = -3.0$ rad	$\phi_{proc} = -3.07$ rad
$d_{FC,2}$	+1 Hz	Tanh	Tanh
		$A/2\pi = +100$ Hz	$A/2\pi = -100$ Hz
		$\phi_{proc} = 2.51$ rad	$\phi_{proc} = 2.36$ rad
$d_{FC,3}$	0 Hz	Tanh	Tanh
		$A/2\pi = +100$ Hz	$A/2\pi = -100$ Hz
		$\phi_{proc} = 1.56$ rad	$\phi_{proc} = 1.41$ rad
$d_{FC,4}$	-2 Hz	Tanh	Tanh
		$A/2\pi = +100$ Hz	$A/2\pi = -100$ Hz
		$\phi_{proc} = 1.10$ rad	$\phi_{proc} = 0.97$ rad
$d_{FC,5}$	-4 Hz	Tanh	Tanh
		$A/2\pi = +100$ Hz	$A/2\pi = -100$ Hz
		$\phi_{proc} = 0.25$ rad	$\phi_{proc} = 0.12$ rad
d_{on-res}	0 Hz	$\tau = 40$ ms	N/A
		$\phi_{proc} = 1.11$ rad	
		$\omega_i = 2104$ Hz	

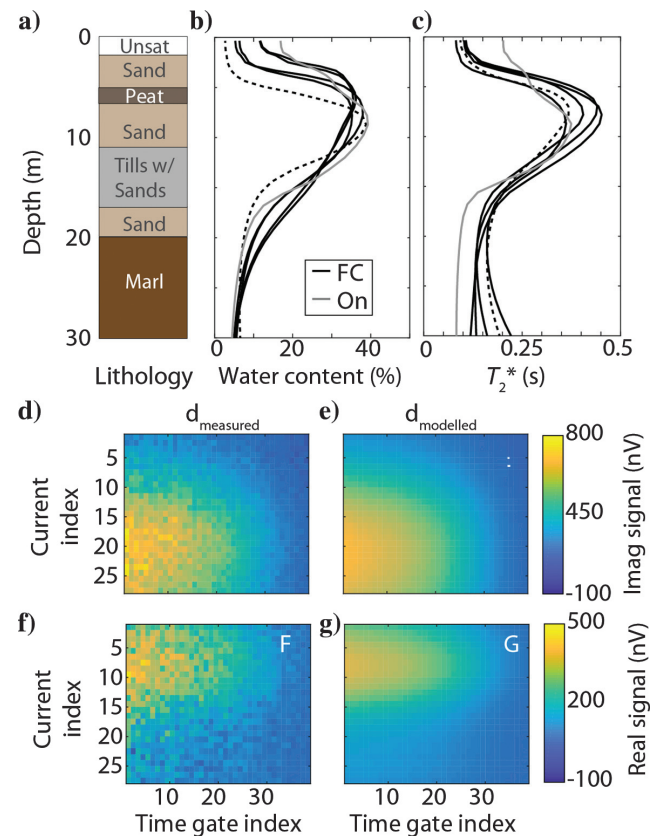


Figure 6. (a) Lithology log describing the subsurface at the hydrogeologic test site Schillerslage near Hanover, Germany. (b and c) Illustrate the estimated water-content and T_2^* profiles. The six profiles shown in (b and c) correspond to the six data sets discussed in Table 1. The four solid black lines correspond to frequency-cycling results that produced satisfactory data fits. The dashed black line illustrates another frequency-cycling result (-4 Hz unknown offset) that produced a poorer data fit and should thus be treated with greater uncertainty. The gray line corresponds to the results of a 40 ms on-resonance survey. (d and f) Illustrate the imaginary and real frequency-cycled data for the +3 Hz unknown offset case. (e and g) Illustrate the imaginary and real modeled data for the frequency-cycling inversion performed using the relevant profiles in (b and c).

frequency resolution, or a poor S/N, it is important to consider that the estimated Larmor frequency may be distinct from the true Larmor frequency. Neglecting the presence of an unknown offset degrades the accuracy of the forward model and limits the ability to accurately reproduce the true water-content profiles while robustly fitting the data. The same artifacts observed when unknown offsets are neglected in the context of a single-frequency pulse survey are also observed when using AHP pulses. For example, unknown offsets can lead to the presence of elevated water contents at depth (Legchenko, 2005) or the presence of spurious features that may be misinterpreted as a subsurface structure. Unknown offsets can also lead to inaccurate estimates of layer boundaries and intralayer water contents. In some cases, the data fit provides evidence that an unknown offset may be present (via a poor data fit), but in certain more insidious cases, the inversion is able to produce good data fits by introducing erroneous features into the water-content profile. The quality of the data fit in these cases would give no reason to suspect that the profile may contain spurious features, which will ultimately lead to biased/poor interpretations of the subsurface.

The advantage of the frequency-cycling scheme is that it is capable of ensuring the accuracy of the forward model, thus improving the reliability of the estimated water-content profiles, without requiring more precise determination of $\omega_{0,\text{true}}$. The frequency-cycling protocol is similar in concept to phase-cycling schemes that are widely used in other NMR disciplines (Bain, 1984), where data acquisition is conducted in a manner that allows one to coherently stack a desired component of the signal while destructively combining undesired components. In our case, the desired component is the portion of the signal accurately described by modeling based upon $\omega_{0,\text{est}}$, whereas the undesired component is the portion that arises from the unknown offset. The frequency-cycling approach does not require increased survey times, but it is able to significantly mitigate the influence of nonzero $\Delta\omega_{\text{un}}$ in exchange for two additional simple steps in the processing workflow: specifically that the processing phase is accounted for and that the data be stacked in the manner described by equation 3. The range of $\Delta\omega_{\text{un}}$ that can be mitigated depends on the particular excitation pulse, a range of ± 3 Hz can be mitigated for the investigated hyperbolic tangent pulse; $\Delta\omega_{\text{un}}$ larger than this range will begin to degrade the accuracy of the estimated water-content profiles. An additional advantage of the frequency-cycling scheme is that it stabilizes the complex inversion by reducing its sensitivity to $\Delta\omega_{\text{un}}$. This improved stability has the potential to facilitate broader implementation of the complex inversion for AHP pulses, allowing resolution improvements provided by the complex inversion to be more widely exploited.

Successful implementation of the frequency-cycling protocol requires accurate absolute-phase estimates for each stacked data set (i.e., d_{+A} and d_{-A}), thus, ensuring that the data are combined in the correct manner during frequency cycling. One challenge is that standard data acquisition/processing protocols impart an additional phase on the measured data called the processing phase, which is typically assumed to be constant for the full data set if the processing steps are unchanged (i.e., across all pulse moments). The processing phase can be estimated as a first step in the inversion process (which is done in this study) (Müller-Petke et al. 2016), or it can be manually estimated (Roy and Lubczynski, 2014). However, this step may introduce an error in the phase of each data set because reliable absolute phases are difficult to produce for an uncertain Larmor frequency estimate. If the processing phase is not

reliably calculated, it will degrade the performance of the frequency-cycling approach, likely resulting in a slightly underestimated water-content estimate (Grombacher et al., 2016). If an approach capable of explicitly modeling/calibrating all contributions to the processing phase is used, these concerns are negated. A discussion about how the processing phase is estimated in this study and how the conductivity term in the forward model must be altered when using frequency cycling is found in Grombacher et al. (2016).

For optimal performance of the frequency-cycling approach for AHP pulses, the data acquisition should be performed to minimize the time separation between the $+A$ and $-A$ data sets that will be

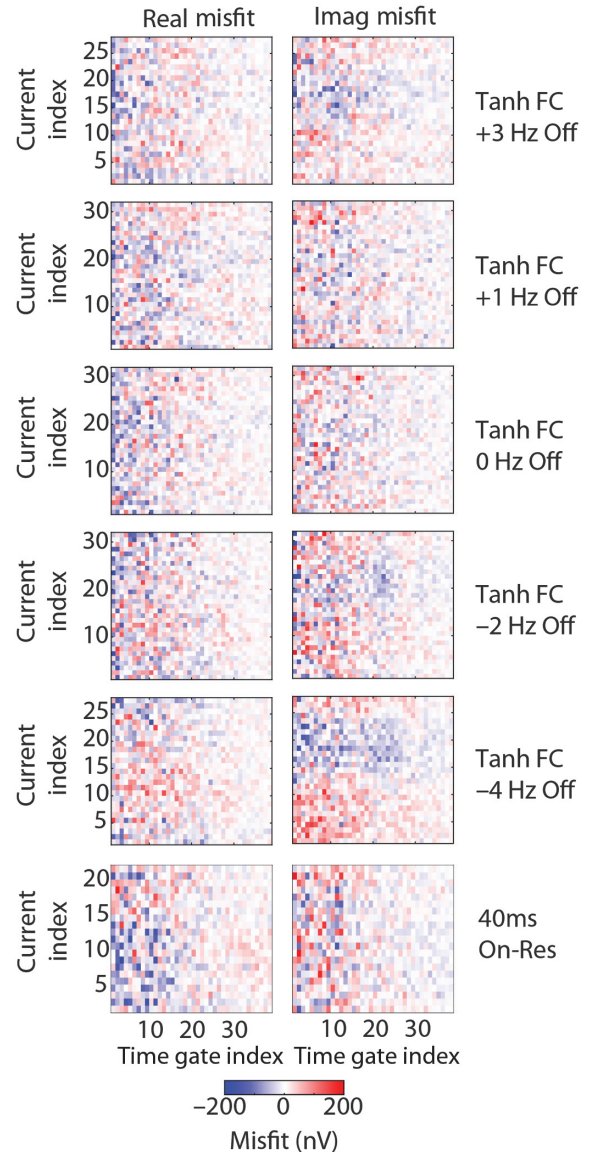


Figure 7. The real (left column) and imaginary (right column) data misfit for each of the six inversion results illustrated in Figure 6b and 6c. The relevant unknown offset is indicated at the right of each row. The top five rows correspond to the frequency-cycled data, whereas the bottom row corresponds to the on-resonance data misfit. High-quality data misfits correspond to randomly distributed red/blue values with a mean of 0 nV. All figures use the same color scale.

combined through frequency cycling. Minimizing the temporal separation will improve the ability of the frequency-cycling approach to mitigate the influence of $\Delta\omega_{\text{un}}$ that arises from temporal \mathbf{B}_0 variations. If significant \mathbf{B}_0 variations occur between the collection of the +A and -A data sets, the accuracy of the frequency-cycling approach will be reduced. To minimize the time separation between +A and -A data sets in the presented field study, the sweep direction was alternated each stack; that is, odd stacks correspond to +A whereas even stacks correspond to -A. A second consideration for frequency-cycling AHP pulses is to ensure that the transmit coil is tuned to $\omega_{0,\text{est}}$. This ensures that the current amplitude modulation during the AHP pulse is the same for the +A and -A frequency sweeps for approaches that use the tuned transmit coil's frequency response to passively modulate the current amplitude during the pulse.

Note that if an AHP data set is collected in the presence of an unknown offset, or if the unknown offset is identified after data collection, reliable water-content profiles may still be produced even if the frequency-cycling approach is not used. In this case, it is important that the data are forward modeled using the best estimate of the offset between the final frequency of the sweep and the Larmor frequency. However, we recommend that the frequency-cycling approach still be used because it can produce reliable results given an uncertain Larmor frequency or a spatially varying Larmor frequency as long as the unknown offset is not so large that the frequency-cycling approach will break down (Grombacher et al., 2016).

CONCLUSION

Producing reliable water-content profiles using surface NMR technique demands accurate modeling of the excitation process. One challenge affecting the accuracy of the forward model is an uncertain Larmor frequency estimate, which can lead to the presence of unknown off-resonance effects that impact the signal amplitude, phase, and spatial origin, ultimately degrading the accuracy of the estimated water-content profile. A frequency-cycling scheme intended for use with AHP pulses is presented to mitigate the influence of an unknown offset between the true and estimated Larmor frequencies. Combining two data sets, one collected using an AHP pulse that starts at a negative offset and a second data set collected using the same adiabatic excitation pulse except for a positive offset, can greatly reduce the impact of an unknown offset between the true and estimated Larmor frequencies. Synthetic and field results demonstrate that unknown offsets as large as ± 3 Hz can be mitigated using the investigated hyperbolic tangent pulse. The frequency-cycling approach is shown to enhance the accuracy of the surface NMR forward model and is capable of producing robust data fits for the amplitude-only and complex inversions. These improvements do not require increased survey times, but they do demand that the phase of the measured data is accurately known. Overall, the frequency-cycling approach offers great potential to ensure that reliable water-content profiles are produced by the surface NMR method.

ACKNOWLEDGMENTS

D. Grombacher was supported by an individual post-doctoral grant from the Danish Council for Independent Research (DFF-5051-00002). The authors would like to thank L. Liu and J. Haldrup for help in collecting the field data. MRSmatlab (Müller-Petke et al., 2016) was used for all forward modeling/inversion of surface NMR data.

REFERENCES

- Bain, A. D., 1984, Coherence levels and coherence pathways in NMR: A simple way to design phase cycling procedures: *Journal of Magnetic Resonance*, **56**, 418–427, doi: [10.1016/0022-2364\(84\)90305-6](https://doi.org/10.1016/0022-2364(84)90305-6).
- Bendall, M. R., and D. T. Pegg, 1986, Uniform sample excitation with surface coils for in vivo spectroscopy by adiabatic rapid half passage: *Journal of Magnetic Resonance*, **67**, 376–381, doi: [10.1016/0022-2364\(86\)90447-6](https://doi.org/10.1016/0022-2364(86)90447-6).
- Braun, M., and U. Yaramanci, 2005, Study on complex inversion of magnetic resonance sounding signals: *Near Surface Geophysics*, **3**, 155–163, doi: [10.3997/1873-0604.2005011](https://doi.org/10.3997/1873-0604.2005011).
- Dlugosch, R., 2014, Aquifer characterization using nuclear magnetic resonance: Ph.D. thesis, Technische Universität.
- Dlugosch, R., and M. Müller-Petke, 2017, Application of adiabatic pulses for 1D surface-NMR imaging: Presented at the 30th Symposium on the Application of Geophysics to Engineering and Environmental Problems.
- Garwood, M., and L. Delabarre, 2001, The return of the frequency sweep: Designing adiabatic pulses for contemporary NMR: *Journal of Magnetic Resonance*, **153**, 155–177, doi: [10.1006/jmre.2001.2340](https://doi.org/10.1006/jmre.2001.2340).
- Grombacher, D., 2018, Numerically optimized modulations for adiabatic pulses in surface nuclear magnetic resonance: *Geophysics*, **83**, no. 2, JM1–JM14, doi: [10.1190/geo2016-0574.1](https://doi.org/10.1190/geo2016-0574.1).
- Grombacher, D., A. A. Behroozmand, and E. Auken, 2017, Compensating for relaxation during pulse effects for long pulses and fast relaxation times in surface nuclear magnetic resonance: *Geophysics*, **82**, no. 6, JM23–JM36, doi: [10.1190/geo2016-0567.1](https://doi.org/10.1190/geo2016-0567.1).
- Grombacher, D., and R. Knight, 2015, The impact of off-resonance effects on water content estimates in surface nuclear magnetic resonance: *Geophysics*, **80**, no. 6, E329–E342, doi: [10.1190/geo2014-0402.1](https://doi.org/10.1190/geo2014-0402.1).
- Grombacher, D., M. Müller-Petke, and R. Knight, 2016, Frequency cycling for compensation of undesired off-resonance effects in surface nuclear magnetic resonance: *Geophysics*, **81**, no. 4, WB33–WB48, doi: [10.1190/geo2015-0181.1](https://doi.org/10.1190/geo2015-0181.1).
- Grunewald, E., D. Grombacher, and D. O. Walsh, 2016, Adiabatic pulses enhance surface nuclear magnetic resonance measurements and survey speed for groundwater investigations: *Geophysics*, **81**, no. 4, WB85–WB96, doi: [10.1190/geo2015-0527.1](https://doi.org/10.1190/geo2015-0527.1).
- Irons, T. P., and Y. Li, 2014, Pulse and Fourier transform surface nuclear magnetic resonance: comprehensive modeling and inversion incorporating complex data and static dephasing dynamics: *Geophysical Journal International*, **199**, 1372–1394, doi: [10.1093/gji/ggu323](https://doi.org/10.1093/gji/ggu323).
- Legchenko, A., 2005, Improved modeling of the magnetic resonance signal in the presence of shallow aquifers: *Near Surface Geophysics*, **3**, 121–130, doi: [10.3997/1873-0604.2005008](https://doi.org/10.3997/1873-0604.2005008).
- Legchenko, A., J.-M. Vouillamoz, F. M. A. Lawson, C. Alle, M. Descloitres, and M. Boucher, 2016, Interpretation of magnetic resonance measurements in the varying earth's magnetic field: *Geophysics*, **81**, no. 4, WB23–WB31, doi: [10.1190/geo2015-0474.1](https://doi.org/10.1190/geo2015-0474.1).
- Müller-Petke, M., M. Braun, M. Hertrich, S. Costabel, and J. Walbrecker, 2016, MRSmatlab: A software tool for processing, modeling, and inversion of magnetic resonance sounding data: *Geophysics*, **81**, no. 4, WB9–WB21, doi: [10.1190/geo2015-0461.1](https://doi.org/10.1190/geo2015-0461.1).
- Mueller-Petke, M., and U. Yaramanci, 2010, QT inversion: Comprehensive use of the complete surface NMR data set: *Geophysics*, **75**, no. 4, WA199–WA209, doi: [10.1190/1.3471523](https://doi.org/10.1190/1.3471523).
- Roy, J., and M. W. Lubczynski, 2014, Exploiting the MRS-phase information to enhance detection of masked deep aquifers: Examples from the Netherlands: *Near Surface Geophysics*, **12**, 309–324, doi: [10.3997/1873-0604.2013058](https://doi.org/10.3997/1873-0604.2013058).
- Semenov, A. G., M. D. Schirov, A. V. Legchenko, A. I. Burshtein, and A. Yu. Pusep, 1989, A device for measuring the parameters of an underground mineral deposit: GB Patent 2,198,540.
- Silver, M. S., R. I. Joseph, and D. I. Hoult, 1984, Highly selective $\pi/2$ and π pulse generation: *Journal of Magnetic Resonance*, **59**, 347–351, doi: [10.1016/0022-2364\(84\)90181-1](https://doi.org/10.1016/0022-2364(84)90181-1).
- Tannus, A., and M. Garwood, 1997, Adiabatic pulses: NMR in Biomedicine, **10**, 423–434, doi: [10.1002/\(ISSN\)1099-1492](https://doi.org/10.1002/(ISSN)1099-1492).
- Trushkin, D. V., O. A. Sushakov, and A. V. Legchenko, 1993, Modulation effects in non-drilling NMR in the earth's field: *Applied Magnetic Resonance*, **5**, 399–406, doi: [10.1007/BF03162536](https://doi.org/10.1007/BF03162536).
- Ugurbil, K., M. Garwood, and A. R. Rath, 1988, Optimization of modulation functions to improve insensitivity of adiabatic pulses to variations in B_1 magnitude: *Journal of Magnetic Resonance*, **80**, 448–469, doi: [10.1016/0022-2364\(88\)90241-7](https://doi.org/10.1016/0022-2364(88)90241-7).
- Walbrecker, J. O., M. Hertrich, and A. G. Green, 2011, Off-resonance effects in surface nuclear magnetic resonance: *Geophysics*, **76**, no. 2, G1–G12, doi: [10.1190/1.3535414](https://doi.org/10.1190/1.3535414).
- Weichman, P. B., E. M. Lavelly, and M. H. Ritzwoller, 2000, Theory of surface nuclear magnetic resonance with applications to geophysical imaging problems: *Physical Review E*, **62**, 1290–1312, doi: [10.1103/PhysRevE.62.1290](https://doi.org/10.1103/PhysRevE.62.1290).